Experiments in Fluids (2025) 66:55
https://doi.org/10.1007/s00348-025-03987-1

RESEARCH ARTICLE

Acoustic streaming flow driven about an array of sharp-edged obstacles

Md. Abdul Karim Miah[1] · Michael G. Olsen[1] · Jaime J. Juárez[1]

Received: 30 August 2024 / Revised: 30 December 2024 / Accepted: 29 January 2025 / Published online: 15 February 2025

Abstract

Acoustic streaming is a process that can be used as a flow control mechanism for mixing, sorting, and enhanced transport phenomena. In this work, we present experimental results examining the superposition of acoustic streaming and bulk flow in a microchannel that incorporates an array of sharp-edge obstacles placed uniformly inside the microchannels. In the absence of bulk flow, we perform experiments over a parameter space consisting of obstacle morphology (circle, square, triangle, cross) and input sinusoidal voltage (4–12 V) with a fixed frequency of 5.8 kHz. Microscopic particle image velocimetry (μPIV) measurements yield a velocity range from 37 to 674 μm/s. Importantly, in all shapes, an overall clockwise rotation was found at the right side of the PZT and anticlockwise rotation at the left side of PZT. Although the peak acoustic streaming velocities are different for each shape, we find that the velocity scales nearly quadratically as a function of applied voltage ($U_o \sim V_{\text{app}}^2$), which is consistent with scaling analyses of acoustic streaming in microfluidic systems. A bulk flow of ~ 185 μm/s is imposed on the microchannel at the same time as a 10 V signal. We find that the resulting flow field can be reconstructed by adding the bulk flow field without streaming to the acoustic streaming flow field without bulk flow.

1 Introduction

Acoustic streaming is a transport mechanism resulting from the exposure of a stationary fluid phase to a periodic acoustic or mechanical wave (Laurell and Lenshof 2014). During this process, the wave transfers its kinetic energy to the fluid due to conservation of momentum (Lighthill 1978), which gives rise to the vortices that are characteristic of acoustic streaming. The vortical flow structure that forms through this interaction depends on the incident sound wave characteristics and system parameters, such as geometry and boundary conditions (Ahmed et al. 2020). The ability of acoustic streaming to generate flow structures has found applications in a number of areas, including enhanced transport in porous media (Khasi et al. 2021; Yeh and Juárez 2019), improved fluid mixing (Pothuri et al. 2019; Ahmed et al. 2009), particle sorting (Ng et al. 2016), heat transfer (Vainshtein et al. 1995), chemical synthesis (Elvira et al. 2013; Dong et al. 2017), and modulation of micro-swimmer motion (Kaynak et al. 2017).

Oscillating microstreaming, a subclass of acoustic streaming, is phenomena induced by oscillating boundaries such as bubbles, pillars, and sharp edges (Zhang et al. 2019a; Jalal and Leong 2018; Lieu et al. 2012). Among these, sharp-edge structures have garnered significant attention due to their pronounced ability to induce localized streaming effects (Zhang et al. 2019b, 2020a, b; Huang et al. 2018, 2013; Chen et al. 2021, 2023; Karlsen and Bruus 2015; Pavlic et al. 2023; Doinikov et al. 2020a, b; Wang et al. 2019). As the oscillating microstreaming phenomenon demonstrates, the presence of obstructions or complex boundaries alter flow patterns that induce vortices and could have potential impact on the aforementioned applications. Experimental observations of oscillating microstreaming from sharp-edged structures exhibit the creation of opposite rotational vortices pair due to acoustic wave interaction, when subjected to alternating current or radio frequency excitation (Wei et al. 2023). This oscillating microstreaming exhibits high velocity (Zhang et al. 2019b; Huang et al. 2013; Harley et al. 2024; Ovchinnikov et al. 2014), potentially attributed to centrifugal forces. Moreover, it operates at relatively low acoustic frequencies, making it suitable for microfluidic

✉ Michael G. Olsen
mgolsen@iastate.edu

✉ Jaime J. Juárez
jjuarez@iastate.edu

[1] Department of Mechanical Engineering, Iowa State University, Ames, IA 50011, USA

systems (Huang et al. 2013; Ovchinnikov et al. 2014). The effectiveness of oscillating microstreaming depends on parameters like sharp-edge geometry and applied voltage as well as flow velocity, fluid properties, and acoustic wave characteristics (Lighthill 1978; Chen et al. 2021; Doinikov et al. 2020b; Wei et al. 2023; Zhang et al. 2020c; Nama et al. 2014). Thus far, most research on oscillating microstreaming has focused either on bubble or sharp-edged structures. However, recent work has illustrated that this phenomenon also arises around obstacles located within microchannels (Miah et al. 2023; Ma et al. 2020).

Oscillating microstreaming generated by obstacles located within a microchannel can be applied to a broad class of multiphase flow problems. For example, sound waves are being used as a technology for enhancing access to natural resources located in porous rock (Adeyemi et al. 2022; Otumudia et al. 2022). The enhanced transport that comes from acoustic streaming and other acoustic related forces mobilize ganglia at fluid-fluid interfaces, leading to improved residence times for multiphase processes (Yeh and Juárez 2019; Li et al. 2005). Such enhancement would not be possible without the oscillating pore structures in which the fluids are located (Miah et al. 2023; Yeh and Juárez 2021). Thus, a closer examination of oscillating pore structures and how their shapes influence localized flow would contribute to a fundamental understanding of acoustic-generated transport phenomena within porous media and other confined fluid media.

This investigation utilizes microscopic particle image velocimetry (μPIV) to measure the fluid velocity field observed around four different obstacle types (square, circular, triangular, and cross) located within a microchannel. A 5.8 kHz acoustic field is applied to the channel to generate oscillating microstreaming. Our observations indicate that sharp corners, indeed, serve as sites of vortex generation. Moreover, the experimental observations suggest that the flow field generated by oscillating microstreaming could be decoupled from pressure-driven bulk fluid flow, and thus, the overall velocity field could be represented by the superposition of flow components in a manner that is analogous to potential flow. To test this observation, we performed a series of experiments wherein we superimposed a uniform pressure-driven flow and oscillating microstreaming. Using μPIV measurements, we show that subtracting the uniform flow component from the superimposed experimental observations does reproduce flow fields nearly identical to those observed in experiments in the absence of uniform flow (i.e., quiescent bulk flow). Thus, the novelty of this work lies in the observation that superimposed oscillating microstreaming flow fields can be reconstructed from individual flow components. Furthermore, a substantial fraction of the available literature on oscillating microstreaming focuses on flow generation due to oscillating sidewall structures (Jalal and Leong 2018). This work differs from previous work by examining flow structures generated by shaped obstacles located within the center of the channel as opposed to the sidewall. Overall, the results presented here can aid the development of microfluidic devices that actively modulate fluid flow, enhance transport phenomena, and sort or assemble particles.

2 Materials and methods

2.1 Micromodel preparation

The microchannels used in this investigation contain four different obstacle geometries (square, circular, triangular, and cross). The microchannels represent porous media micromodels with the obstacles representing pore grains. Each shape is inscribed within a 200 μm diameter circle. Obstacles were positioned within the microchannels, spaced 620 μm apart in both the transverse and longitudinal directions. The circular shape has a diameter of 200 μm. The triangular shape inscribed within a 200 μm diameter circle is an equilateral triangle with each edge length of 173 μm. The edge lengths of square shape inscribed within a circular diameter of 200 μm is 141.42 μm. For the cross shaped obstacles, each of the four arms extends outward with a length and width of 64 μm.

The microchannels are prepared using photolithography. In brief, the microchannel is designed using AUTOCAD to create a photomask for photolithography. An example of the microchannels used in this study, illustrated in Fig. 1, feature obstacles set within a 2 mm wide, 20 mm long, and 50 μm deep channel (the depth is defined by the thickness of the photoresist layer, as described below). The microchannel CAD files were printed as an optically clear photomask by Fineline Imaging, Inc.

SU-8 2050 photoresist was poured onto a 100 mm-diameter silicon wafer (University Wafer, catalog # 452) and spun at high speed to create a uniform thin film. The specific parameters for this process, including spin rates, baking times, and UV energy exposure, are detailed in Table 1. These parameters resulted in a uniform ~ 50-μm-thick film across the wafer's surface. Following the post-exposure bake, the wafer underwent a 3-min immersion in SU-8 developer to eliminate unwanted portions from the wafer. The wafer then underwent a 10-min high-temperature bake at 150 °C. The baking step was followed by exposure to a silane vapor for 2 h within a desiccator using 1H,1H,2H,2H-perfluorooctyl-trichlorosilane. This silanization step was executed to facilitate the easy removal of casting material from the silicon wafer mold.

The silicon wafer molds of the microchannels were replicated using polydimethylsiloxane (PDMS). PDMS

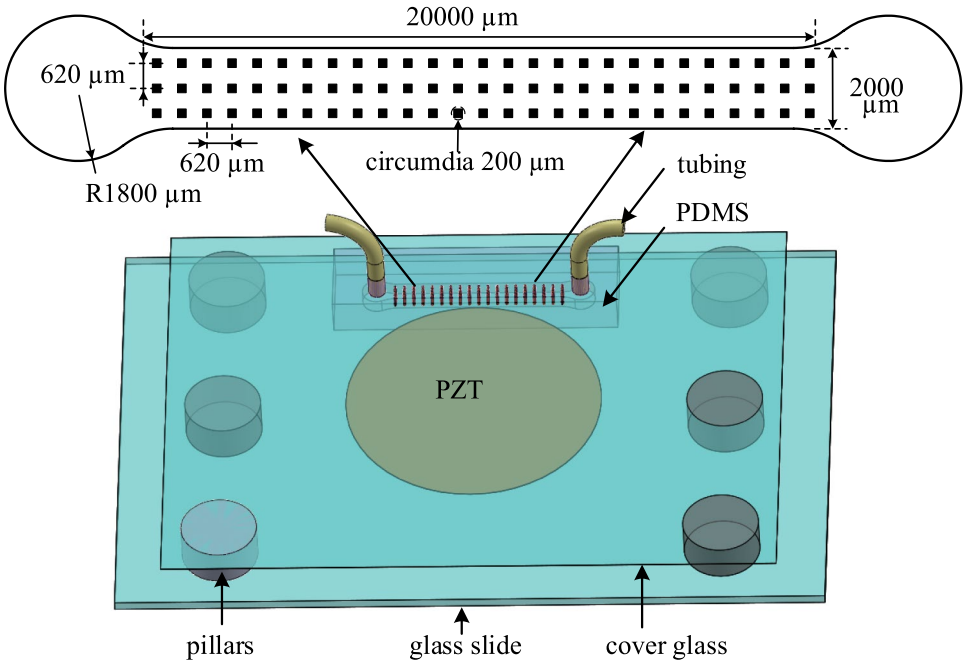

Fig. 1 The figure illustrates the micromodel with square-shaped obstacles employed in the experiment. A PZT is affixed beneath the cover glass, to which the channel is adhered. The device is upheld by six silicon pillars. The inset above provides details of the channel's dimensions

Table 1 Parameters used in photolithography

Photoresist	SU-8 2050
Thickness	50 µm
Spin coating (RPM and Time)	500 RPM for 5 s at acceleration of 100 RPM/s 3000 RPM for 35 s at acceleration of 300 RPM/s
Soft bake times	3 min at 65 °C and 7 min at 95 °C
Exposure energy	195 MJ/cm^2
Post-exposure bake times	2 min at 65 °C and 8 min at 95 °C

was prepared by thoroughly mixing PDMS monomer and curing agent in a 10:1 ratio, respectively. Bubble removal was accomplished by degassing the PDMS mixture before pouring it into a 100 mm petri dish containing silicon wafer molds. The PDMS-filled petri dish was heated to 42 °C for 5 h to promote monomer crosslinking. Once the curing process was complete, a razor was used to remove the channel mold from the wafer.

A biopsy punch was used to create inlet and outlet holes in the reservoirs at both ends of the device to facilitate fluid flow. The PDMS was bonded to 48 mm × 65 mm cover glass (Thermo Scientific, Catalog No. 48X60-1-002G) using a plasma chamber (Harrick Plasma, model no. PDC-32G), wherein the PDMS and cover glass were placed upright in the chamber and exposed to the highest radio frequency (RF) setting for 45 s. The two substrates were removed from the chamber and brought into contact with each other to establish a strong bond. Adhesion between the PDMS and cover glass was enhanced by heating the device to 100 °C for 10 min. Finally, silicone tubes (US Plastics, catalog # 57286) were inserted into the inlet and outlet holes of the reservoirs, and a small quantity of PDMS was applied around the holes to act as a sealant.

A 27-mm-diameter piezoelectric transducer (PZT) was sourced from Digi-Key (Product No. 668–1407-ND) and served as an acoustic generation element. The PZT had a manufacturer-reported unloaded resonant frequency of 4.6 kHz. Before performing plasma bonding, a marker pen was used to mark the position of the PZT and channel on the cover glass so that PZT is placed exactly at the center of the cover glass and channel is placed very close to the PZT on the opposite side of cover glass. 5-min epoxy (Gorilla Glue, Catalog No. 4200102) was used to bond the PZT to the cover glass. The PZT bonding process was followed up by bonding silicone pillars (Amazon, catalog no. BE20SL100005-100P), 3.8 mm height, to the cover glass. The silicone pillars were then glued to a larger glass slide (75 × 50 × 1 mm, Fisher Scientific, Catalog No. 12-550C) using epoxy. Owing to uniformity of the silicone pillars, we assumed that microchannel is completely horizontal. The entire assembly was then placed in a particle-free cabinet and allowed a minimum of 24 h for the epoxy to fully cure before any experiments were conducted. The complete assembly is depicted in Fig. 1.

2.2 Fluid sample preparation

Fluorescent polystyrene particles, measuring 1 µm in diameter, served as the seed particles for the microscopic particle image velocimetry (µPIV) experiments. These fluorescent

tracer particles, obtained from ThermoFisher Scientific (F8852, lot No. 1795381), possessed excitation and emission wavelengths of 505 nm and 515 nm, respectively. To enable the tracking of streaming phenomena within the channels, the fluorescent tracer particles were introduced into water at a concentration of 0.05% by volume.

2.3 Experimental methods

Microscopic particle image velocimetry (μPIV) experiments were conducted with an inverted fluorescent microscope (Olympus IX70). In experiments involving pressure-driven flow, a 1/16" nylon barb fitting (Fisher Scientific, Catalog No. 50–255-8409) served as an interface between the device inlet and silicone tubing that introduces fluid to the device. Fluid was introduced using a syringe pump (Chemyx, Fusion Touch Series Model 740). Silicone tubing was also affixed to the outlet port on the opposite side of the device, with sufficient length to direct effluent into a glass beaker, which acts as a fluid collector. The shortest feasible length of tubing was utilized to minimize hydraulic capacitance's influence on the experiments.

For experiments in quiescent water, the channel was initially cleansed with deionized (DI) water. Fluorescent particle-seeded water was then introduced into the channel, ensuring that the entire channel and reservoir were filled. Special attention was paid to prevent bubble entrapment within the channel, as bubbles would disrupt acoustic streaming. Subsequently, acoustic signals were generated using a function generator, varying voltage levels at different frequencies to identify the resonance frequency which causes maximum streaming intensity. Data was recorded using a camera at this resonance frequency. In experiments involving pressure-driven flow, fluorescent particle laden water was delivered into the channel through the inlet using a pressure pump and syringe. The acoustic signal was then transmitted once the flow had reached a steady state.

Figure 2 depicts the schematic of the experimental configuration. The experimental setup comprises of a device assembly situated on the Olympus IX70 microscope stage. A Tektronix AFG1022 function generator applied varying peak-to-peak sinusoidal voltages at frequencies around 5.8 kHz, which our experiments suggest is the loaded resonant frequency of the PZT. Amplification of the acoustic signal was achieved using an RF amplifier (Amplifier Research, model 50A220). Signal frequency and amplitude were monitored using a Tektronix TBS 1052B-EDU oscilloscope. Image acquisition was performed with a 2.3-megapixel monochrome camera (Teledyne FLIR, model GS3-U3-23S6M-C) at a data collection rate of 160 frames per second (FPS).

The acquired images underwent preprocessing through the application of image masks to eliminate undesired regions within the images. Specifically, it was observed that the presence of the obstacles in images, which were devoid of seed particles, led to the generation of erroneous vectors. The analysis of images to determine the steady-state velocity field was performed using the open-source software PIVlab, a Digital Particle Image Velocimetry Tool for MATLAB (Thielicke and Stamhuis 2014). This software relies on the discrete Fourier transform algorithm to compute velocity fields through the cross-correlation method (Raffel et al. 2007; Westerweel 1997).

For steady-state scenarios, the ensemble cross-correlation technique was employed to interrogate the images to extract velocity fields. Each experiment involved the analysis of approximately 750 images. In the case of 4× magnification images, a multi-pass interrogation procedure was applied with a final interrogation spot area measuring 24 pixels by 24 pixels (1 pixel = 1.433 μm) and a step size of 12 pixels between adjacent interrogation spots, resulting

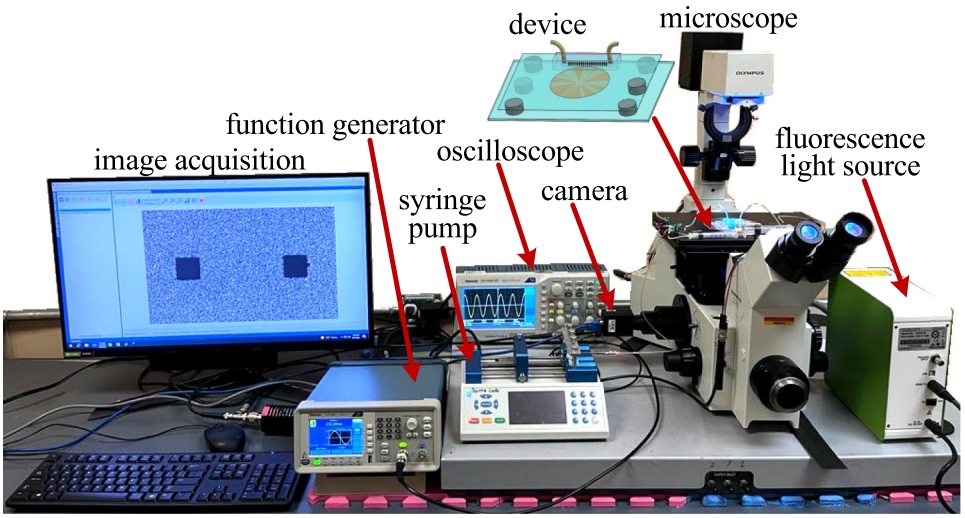

Fig. 2 A schematic illustrating the experimental configuration employed for μPIV experiments within microchannels featuring various types of obstructions

in a 50% overlap between them. For 10 × magnification, the final interrogation area was 40 pixels by 40 pixels (1 pixel = 0.575 μm), with a step size of 20 pixels. For 20 × magnification, the final interrogation area was 48 pixels by 48 pixels (1 pixel = 0.29 μm), with a step size of 24 pixels. Standard correlation robustness was employed (Thielicke and Sonntag 2021).

For 4 × magnification, the final vector map featured an in-plane spatial resolution of 17.20 μm (smallest interrogation size of 12 pixel corresponds to 17.2 μm). The out-of-plane spatial resolution encompassed the entire depth for 4 × measurements. In the case of 10 × magnification, the final vector map had an in-plane spatial resolution of 11.50 μm, with an out-of-plane spatial resolution of 25 μm. For 20 × magnification, the final vector map exhibited an in-plane spatial resolution of 6.95 μm, with an out-of-plane spatial resolution of 14.46 μm (Bourdon et al. 2004, 2003; Olsen and Adrian 2000).

An example PIV image with vectors is shown in Fig. 3. The image was captured at 10 × magnification. The vectors were found after the cross-correlation of 750 PIV images in PIVlab as described above.

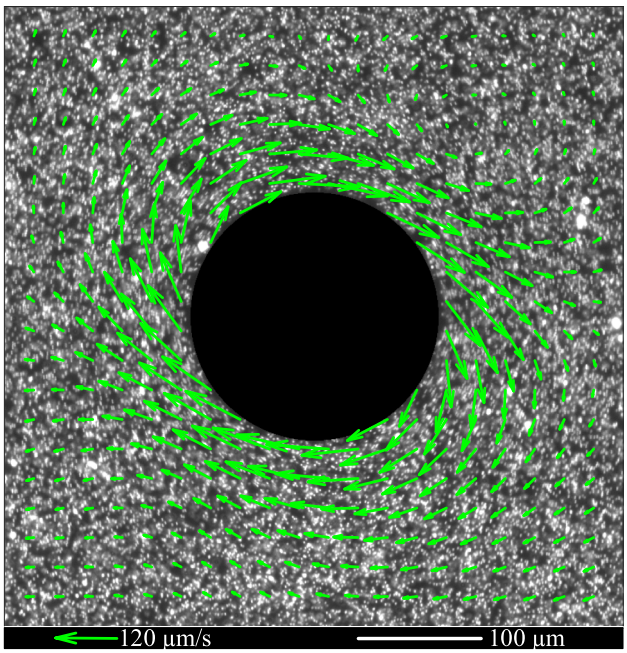

Fig. 3 An example PIV image with velocity vectors found after image interrogation. For clarity, only one out of each four vectors have been shown (i.e., the actual velocity field contains 4 times the number of vectors shown) for streaming in the right position of the channel at 8 V. Images were captured at 10X magnification. Fluorescent tracer particles have been introduced into water at a concentration of 0.05% by volume

3 Results and discussion

Acoustic streaming experiments in quiescent water were performed for three distinct sharp-edged obstacle geometries: square, triangular, and cross-shaped. Experiments were also performed using a circular obstacle as an experimental control. We examined a range of frequencies encompassing the following intervals: squares (5.2–9.0 kHz), circles (4.9–7.8 kHz), triangles (4.8–7.8 kHz), and crosses (4.9–9.8 kHz). The strongest response occurred at a resonant frequency of 5.8 kHz for channels with circular, triangular, and square-shaped obstacles, while the channel with cross-shaped obstacles exhibited a resonance frequency of 5.6 kHz. No discernible circulation around the obstacles was observed beyond the aforementioned frequency ranges. Once the resonant frequency was identified, we performed experiments at this frequency using peak-to-peak sinusoidal voltages of 4 V, 8 V, and 12 V. Data at these voltages were acquired at three distinct locations within each channel containing the same type of obstacle: the center directly opposite the PZT; to the right of center at a distance of 5.58 mm; and, to the left of the center at a distance of 5.58 mm. Representative examples of experimentally measured velocity fields, featuring a channel with square-shaped obstacles, are illustrated in Fig. 4 and were captured using a 4 × magnification.

Experiments with square obstacles at the center position, shown in Fig. 4, revealed the generation of two counter-rotating vortices at each corner when the channel is actuated at the resonant frequency. This is consistent with previous observations in the literature where counter-rotating vortices have been found around sharp corners (Zhang et al. 2019b, 2020a, c; Huang et al. 2013; Chen et al. 2021). The rotation is strongest at the mid-width of the channel where each vortex originates near the corner and travels along the edge of the square until it reaches the midpoint. Vortices on the same side of the square rotate in opposite directions and meet at the square midpoint, after which the fluid flows away from the square. The strength of these counter-rotating vortices is approximately equivalent. The fluid velocity in the space between the obstacles is zero, indicating the streaming is localized to the obstacles. Moving away from the mid-width obstacles along the transverse direction (i.e., across the channel width) sees vortex intensity diminish, although several weak vortices remain present at the corners.

To the left of the center position in the longitudinal direction (moving down the long axis of the channel) (Fig. 4), acoustic streaming generated at the resonant frequency leads to four individual vortices at each corner for the obstacles. Unlike their counterparts in the center

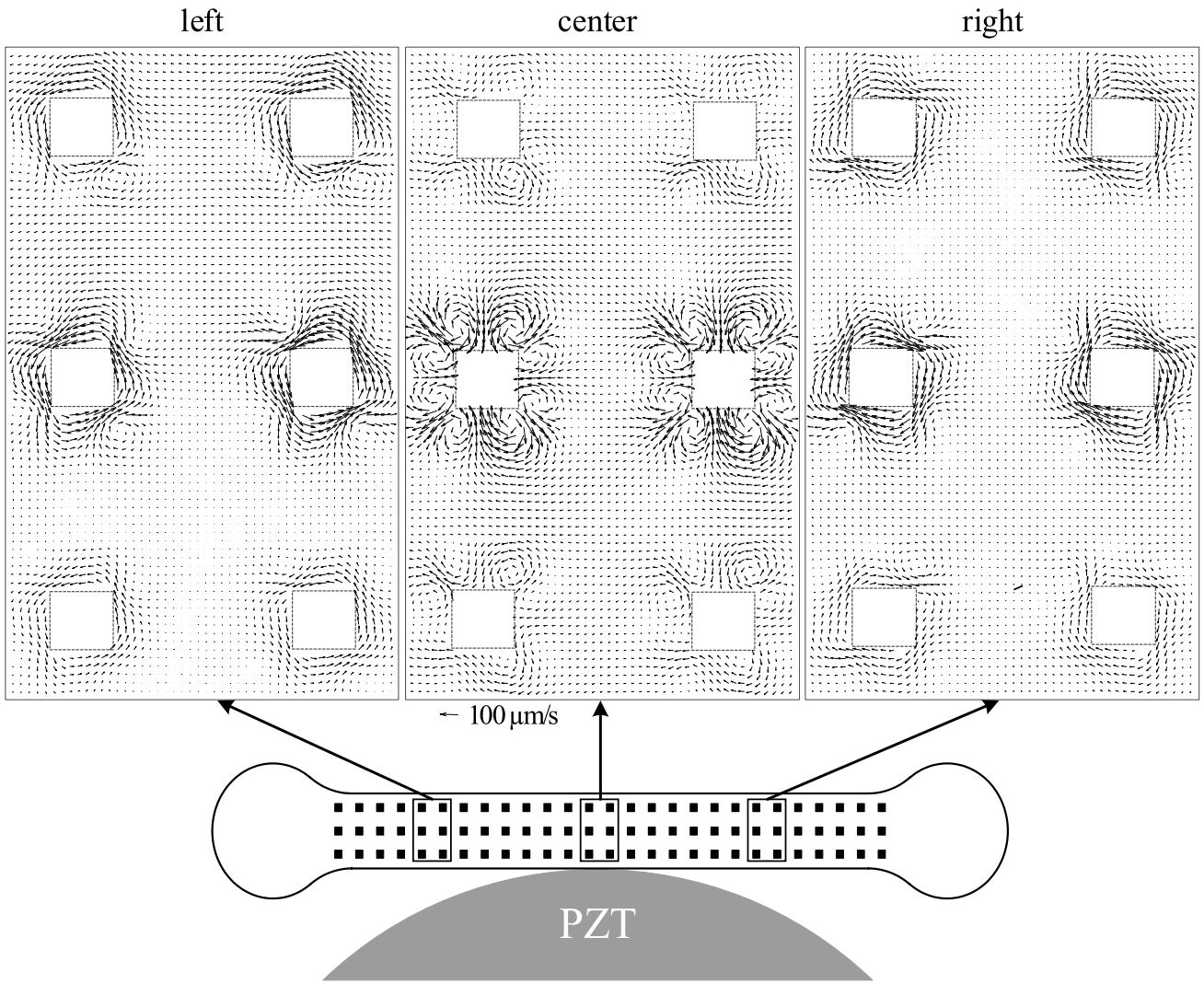

Fig. 4 Measured velocity fields at the left, center, and right positions in the channel with square obstructions for 8 V acoustic signal at 5.8 kHz. Images were captured at 4 × magnification

position, these square obstacles appear to transition from having eight vortices to a single vortex that circulates around the obstacles at this location. Another, smaller vortex is located just below the larger vortex near several of the obstacles. The circulation at this location does not appear circular but is almost square shaped with rounded corners (i.e., a hypotrochoid square). Furthermore, this hypotrochoid square is oriented with a slight counterclockwise rotation. Conversely, the streaming behavior to the right of the center position appears as a mirror reflection of the left position at equal distances, creating symmetrical characteristics. Unlike the flow on the left, the flow on the right circulates clockwise. Overall, local vorticity strength and quantity is most pronounced at the center of the channel but diminishes as one moves away from the center in the longitudinal direction.

We extended our observations to three other obstacle geometries, as illustrated in Fig. 5. The μPIV measurements were performed at the same voltage as those done in the square obstacle case. As discussed above, the resonance frequency was the same 5.8 kHz signal for each obstacle, except for the cross, which exhibited a 5.6 kHz resonance frequency. We observed distinct differences between each of the obstacles examined in our experiments. The circular obstacle (second top, Fig. 5) exhibits no discernible circulation at the channel centerline (column B). Moving left of the center (column A), we observe counterclockwise circulation, whereas circles located to the right of the center (column C) exhibit clockwise circulation. We note that the rotational flow structure appears to exhibit an elliptical shape rather than the circular shape of the obstacle. This is likely the result of interactions with the acoustic source as the surface

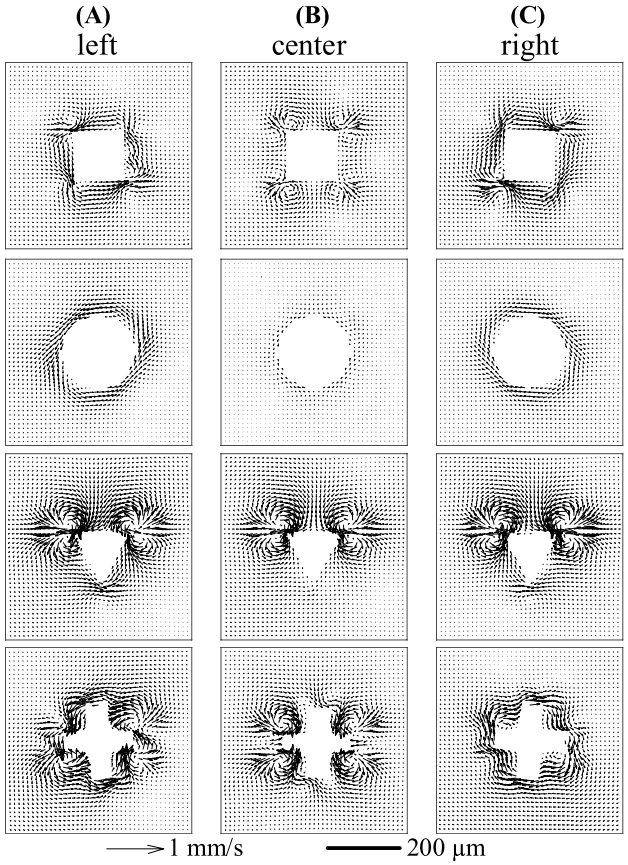

Fig. 5 Measured velocity fields around different shaped obstructions in the microchannels for 8 V acoustic signal at resonant frequency. **A** streaming in the left position, **B** streaming in the center position, **C** streaming in the right position

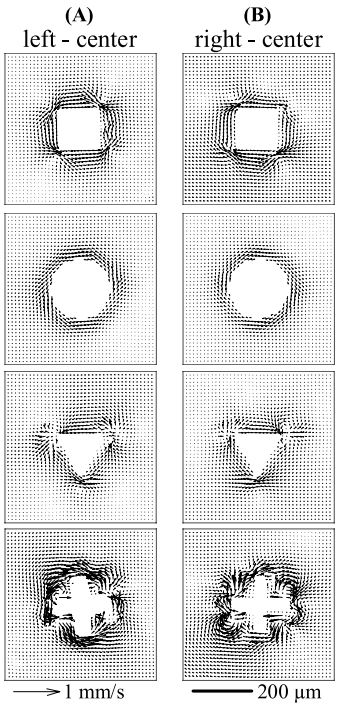

Fig. 6 Measured velocity fields around different shaped obstructions in the microchannels for 8 V acoustic signal at resonant frequency. **A** deviation of streaming in the left position from center position, **B** deviation of streaming in the right position from center position

waves propagate outward from the channel center. The rotational behavior is consistent with our previous work (Miah et al. 2023), however, contrasts with the results of Lieu et al. (2012) where counter-rotating vortices were observed. A significant difference between these results and those of Lieu et al. is the use of two PZT elements as opposed to one in this work. The waves generated by two PZT elements vibrating simultaneously will interfere with each other, which likely contributes to those contrasting observations.

The triangle structure in the centerline position exhibits no flow at the vertex facing down, while the two vertices on the top of the triangle are observed to feature strong oscillatory microstreaming. Each vertex features a counter-rotating vortex pair, similar to those observed with the squares. The vortices at the top bring flow toward the top face of the triangle. The fluid then accelerates as it moves away from the face in a direction that is perpendicular to the direction in which it was first brought in. Moving to the left of the center, we see the vortex flow change slightly with more fluid flowing to the vertex on the upper left. While this fluid continues to primarily eject fluid away from the upper face of the triangle, some of this fluid flows back toward the face on the lower left side of the triangle. This fluid then continues flowing along the face until it reaches the bottom vertex, where the flow changes direction and flows back up the right triangle face. Indeed, the flow structures here resemble the source-sink pairs. In column A of Fig. 6, which measures the deviation of left position from the center position, shows that an overall anticlockwise motion is being added with some corner vortices as one goes from center to the left. The flow structures observed to the right of the center continue to mirror those on the left.

In the center position, the cross-shaped obstacles (Fig. 5, bottom) feature vortices where the faces of the cross-meet at right angles. As with the squares, the fluid is drawn in toward the faces at the top and bottom before streaming away on either side of the cross. To the left (position A), the vortices disappear and are replaced by a flow structure that resembles a source-sink pair. The source appears on the upper rightmost vertex of the cross, sending fluid away from this point and sending streaming counterclockwise around the cross. The vertex below the upper rightmost vertex resembles a sink, drawing fluid toward this point. In column A of Fig. 6, which measures the deviation of streaming in left position from center, an overall anticlockwise circulation of fluids has been found around the shape. It indicates that an overall anticlockwise circulation is added to the center

streaming as one moves from center to the left. Unlike the other shapes examined in this work, the flow structure to the right of center (positions C of Fig. 5) does not appear to mirror the flow structure on the left. At position C, the flow appears to circulate around the cross, as it has done with other shapes. The difference between flow structures suggests that the cross-shape may be breaking the flow symmetry to some extent. In column B of Fig. 6, which measures the deviation of streaming in right position from center, an overall clockwise circulation of fluids has been found around the shape.

The maximum oscillatory microstreaming velocity observed in our experiments varied based on shape type. Circular obstacles featured the lowest maximum velocity among our experiments, followed in ascending order by triangle, square, and cross. The oscillatory microstreaming velocity is also sensitive to voltages applied to the PZT. Higher voltages consistently generate higher streaming velocities. We note that the maximum oscillatory microstreaming velocity is highest to the left or right of the center position for the circular obstacles, where the velocity is nearly zero. However, the triangle, square, and cross-obstacles feature their highest velocities in the center for the channel. Based on an expression for the characteristic fluid velocity (Barnkob et al. 2012), $U_o = 4E_{ac}/\rho_f c_f$, and an anticipated scaling (Barnkob et al. 2010) of $E_{ac} \propto V_{app}^2$, we expect our own data to follow a similar trend. Table 2 shows the maximum velocity measured for each of the obstacle types in our experiments. Data was collected at three voltages for each obstacle type. This table shows that circular obstacles consistently exhibit the lowest velocities at each voltage. Previous studies (Chen et al. 2021; Zhang et al. 2020b) have indicated that triangular geometries, due to their acute tip angles, generate higher streaming velocities compared to square and cross-shaped structures. Our current findings align with this understanding, as we observe that triangular shapes exhibit greater streaming velocities than square ones. However, our observation that cross-shaped structures produce even higher streaming velocities than triangular one's contrasts with earlier research. This discrepancy can be attributed to our consideration of internal obstacles within the structures, suggesting that streaming phenomena are influenced by the overall device architecture, differing from previous studies that may not have accounted for such complexities. We fit the current data to a power law function of the form $U_o = aV_{app}^b$, where a and b are fitting constants. The exponent, b, appears to be close to the predicted value (Bruus 2012) of 2 for the circle, triangle, and square case. However, the value of b for the cross is lower than the fitted values for the other geometries. This suggests that this particular shape attenuates the acoustic waves generated by the PZT differently from the others. This aligns with our observations of symmetry breaking in the cross-shaped obstacle flow structures. We note that this quadratic scaling is also observed in Ovchinnikov et al. (2014) who showed that the quadratic scaling holds for sharp-edged structures embedded in the sidewall of a channel.

With the characteristics of steady streaming established, we add a pressure-driven bulk flow to better understand how these effects superimpose. For our superposition experiments, we use a pressure-driven flow rate of 60 µL/hr with a 12V, 5.8 kHz acoustic signal. This flow rate yields an average interstitial velocity of $U_f \sim 185$ µm/s. For porous media, the interstitial velocity is defined as $U_f = Q/A\varphi$, where Q is bulk flow rate, A is channel cross-sectional area, and φ is the channel porosity (Holdich 2002). This velocity corresponds to a Reynolds number of 0.026, where using the average interstitial velocity as the characteristic Reynolds number and the channel hydraulic diameter as the characteristic length. By superimposing bulk flow onto a flow generated by acoustic streaming we can define an effective acoustic streaming number, $AS = U_o/U_f$, which compares the acoustic streaming strength to the bulk flow velocity. Figure 7 (bottom) shows this experiment, performed with square obstacles at a maximum $AS \approx 2.3$. The case with an acoustic field input is compared to the absence of an acoustic field (Fig. 7, top). Without steady streaming, the flow field resembles potential flow with an obstacle in the presence of a uniform flow. Moving from left to right (Fig. 7, bottom left), the flow around the obstacle appears to closely resemble the case without a superimposed acoustic field (Fig. 7, top left), although weak vortices appear in the upper left

Table 2 Maximum velocity magnitudes of the circulation around different shaped obstructions

Channel types	Max velocity magnitude at 4 V [µm/s]	Max velocity magnitude at 8 V [µm/s]	Max velocity magnitude at 12 V [µm/s]	Fitting parameters of equation $U_o = aV_{app}^b$	
				a	b
Circular	37	120	282	2.8447±0.1146	1.8324±0.0168
Triangle	90	308	663	7.2368±0.1188	1.8131±0.0068
Square	58	205	424	4.7135±0.1191	1.8119±0.0105
Cross	102	351	674	9.4251±0.1396	1.7257±0.0062

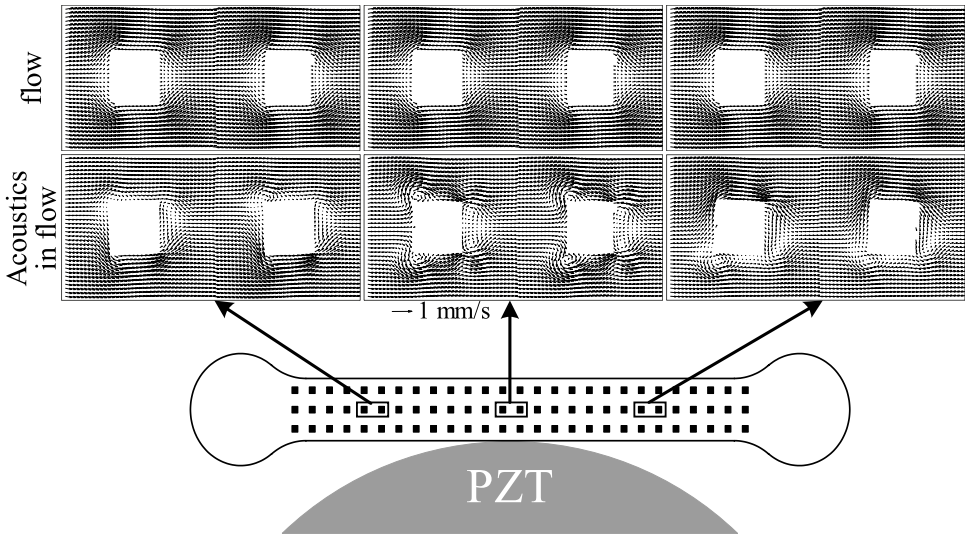

Fig. 7 Measured velocity fields around square obstacle at the left, center, and right position at 60 µL/hr flow (top row), and acoustic impact of 12V signal at 5.8 kHz in the pressure-driven flow of 60 µL/hr (bottom row). The acoustic streaming number is 2.3 for the case of superimposed acoustic fields. Bulk flow is from left to right

square corner. Although these two cases appear indistinguishable at this location, we show using µPIV data that the acoustic field can be reconstructed by subtracting the bulk flow contribution (Fig. 7, top left) from the case where bulk flow and the acoustic field are superimposed (Fig. 7, bottom left). The vortices grow in intensity as we approach the center of the channel in Fig. 7 (bottom), before declining in strength on the right.

In Fig. 8, we expand the examination of superimposed flow effects to the three other shapes examined in our work. The data shown in Fig. 8 are taken from the right most position observed in the channel. In Fig. 8, Column A shows the superimposed effects of pressure-driven flow with a constant flow rate of 60 µL/hr and vortex flow induced by steady streaming at 10 V. Column B of Fig. 8 shows the flow field for uniform flow around the obstacle in the absence of steady streaming. By the principle of superposition, we subtract the flow field shown in Column B from the result in Column A, and the result is shown in Column C. This process yields the flow field contribution of steady streaming. Column D in Fig. 8 shows the flow field of steady streaming found experimentally. Table 3 shows the percentage of the mean of the absolute errors between the calculated streaming and experimental streaming. Indeed, we see that the two flow fields are nearly identical, thus demonstrating the concept that the effects of pressure-driven flow and acoustic streaming can be separated from each other at the Reynolds numbers investigated. This observed phenomenon could have significant consequences in simplifying numerical modeling of flows containing both pressure-driven flow and acoustic streaming, as the two effects could be modeled separately and then superimposed together, as opposed to modeling both effects simultaneously. Decoupling the acoustic mechanisms into separate components that represent bulk flow, oscillatory motion, and steady streaming motion, is a common approach to acoustic streaming model development (Zhang et al. 2019a; Bruus 2011). Indeed, these experiments showcase the utility of this concept to understanding experimental results.

4 Conclusions

In this work, we examine oscillating microstreaming around distinct obstacle geometries (circular, triangular, square, and cross) using microscopic particle image velocimetry (µPIV). Our findings show that vortices preferentially occur near sharp corners, with the cross-shape exhibiting the highest measured velocity (674 µm/s) for a given acoustic source voltage. Circulation was also observed around the circular obstacles, although it yielded the lowest measured velocity (37 µm/s) compared to the other geometries. For all obstacle types, the device architecture influences the direction and magnitude of flow circulation around the obstacle, as dependent on the angular positioning of the obstacles relative to the piezoelectric transducer (PZT), as detailed in our previous work (Miah et al. 2023). Consequently, symmetric flow patterns were observed on either side of the PZT, characterized by clockwise circulation on the right and counterclockwise circulation on the left. While previous work on acoustically generated flows around sharp edges focused on sidewall structures, this work expands on this topic by examining the impact that obstacles embedded within the channel have due to an acoustic field.

We observe that when the flow is driven simultaneously by both a pressure gradient and an acoustic streaming, the contributions of both pressure and acoustic streaming can be separated from one another. We tested this by superimposing a uniform flow field via the introduction of a constant pressure-driven flow rate of 60 µL/hr with acoustic streaming.

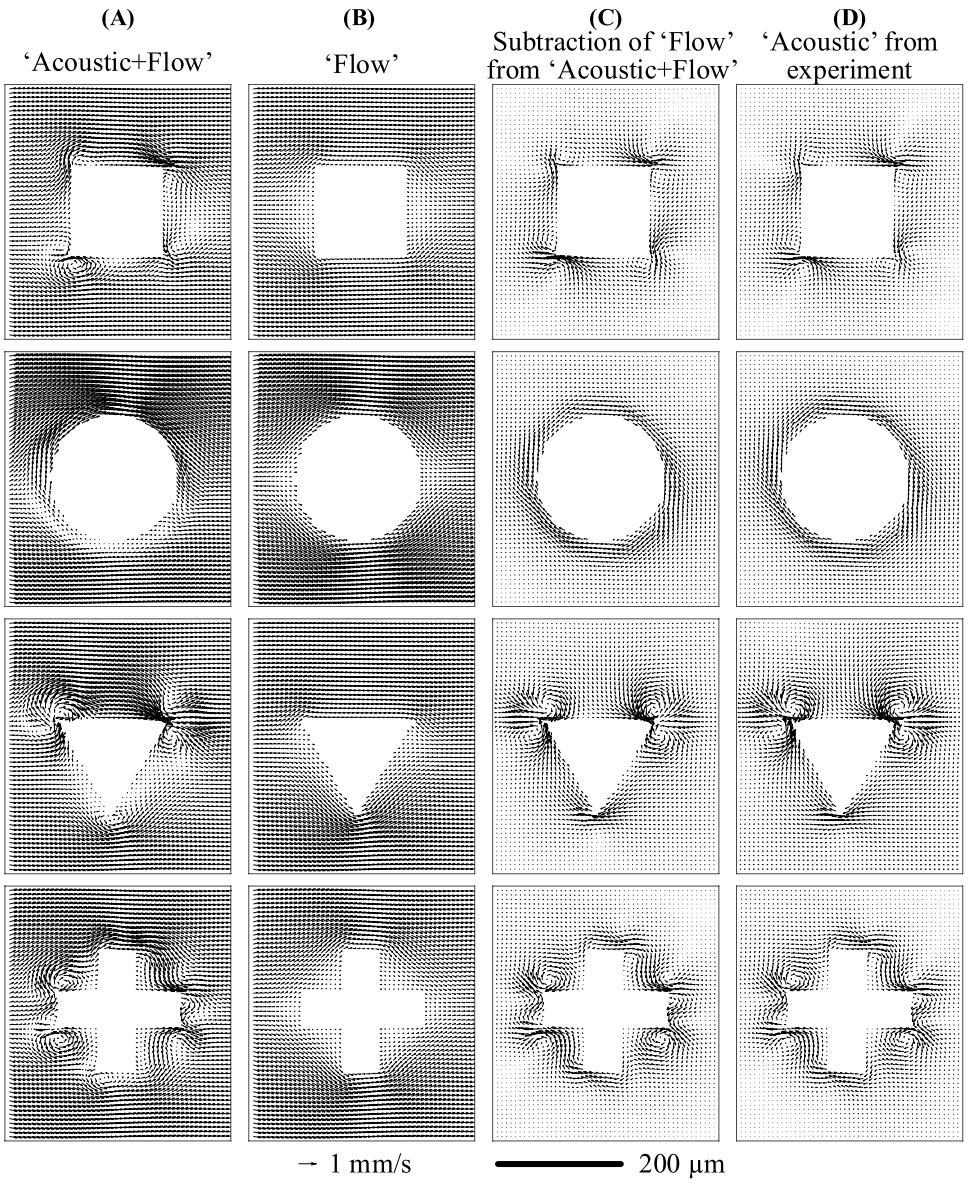

Fig. 8 Superposition principle applied to the channels with four different shaped obstructions in the right position. Flow is from left to right. **A** 10 V acoustic signal at resonant frequency applied to pressure-driven flow of 60 μL/hr, **B** Pressure-driven flow at 60 μL/hr, **C** 10 V acoustic impact calculated by subtracting column B from column A, **D** 10 V acoustic impact at resonant frequency found from experiment

Our experiments show that when we subtract the uniform flow field component from a case where flow and streaming were experimentally observed, the resulting velocity field was nearly identical to the velocity field induced purely by acoustic streaming. This observation will lead to simplified models of oscillating microstreaming under conditions where the streaming component can be considered steady, because the pressure-driven flow and acoustic driven flow can be modeled separately and then simply superimposed, eliminating the need to model both phenomena simultaneously. Furthermore, this work may find applications in a variety of fields, including, but not limited to, microfluidic flow control, heat transfer, and sample mixing.

Table 3 Error between calculated velocities and experimental velocities

Obstruction types	Mean absolute error between experimental acoustic velocities and calculated acoustic velocities (%)
Square	1.65
Circle	3.60
Triangle	2.4
Cross	1.75

Acknowledgments JJJ and MGO gratefully acknowledge the support of the United States National Science Foundation through award number 2050105.

Author contributions MAKM performed the research, prepared all figures, and wrote the first draft. MGO and JJJ supervised the work, obtained funding, and edited the manuscript. All authors reviewed the manuscript.

Data availability All data are provided within the manuscript or has been uploaded as supplementary information.

Declarations

Conflict of interest The authors declare no competing interests.

References

Adeyemi I, Meribout M, Khezzar L (2022) Recent developments, challenges, and prospects of ultrasound-assisted oil technologies. Ultrason Sonochem 82:105902

Ahmed D, Mao X, Juluri BK, Huang TJ (2009) A fast microfluidic mixer based on acoustically driven sidewall-trapped microbubbles. Microfluid Nanofluid 7:727

Ahmed H, Ramesan S, Lee L, Rezk AR, Yeo LY (2020) On-chip generation of vortical flows for microfluidic centrifugation. Small 16:1903605

Barnkob R, Augustsson P, Laurell T, Bruus H (2010) Measuring the local pressure amplitude in microchannel acoustophoresis. Lab Chip 10:563–570

Barnkob R, Augustsson P, Laurell T, Bruus H (2012) Acoustic radiation- and streaming-induced microparticle velocities determined by microparticle image velocimetry in an ultrasound symmetry plane. Phys Rev E 86:056307

Bourdon CJ, Olsen MG, Gorby AD (2003) Validation of an analytical solution for depth of correlation in microscopic particle image velocimetry. Meas Sci Technol 15:318

Bourdon CJ, Olsen MG, Gorby AD (2004) Power-filter technique for modifying depth of correlation in microPIV experiments. Exp Fluids 37:263–271

Bruus H (2011) Acoustofluidics 2: perturbation theory and ultrasound resonance modes. Lab Chip 12:20–28

Bruus H (2012) Acoustofluidics 7: the acoustic radiation force on small particles. Lab Chip 12:1014–1021

Chen Z et al (2021) Sharp-edge acoustic microfluidics: principles, structures, and applications. Appl Mater Today 25:101239

Chen H et al (2023) Experimental study of acoustic streaming induced by a sharp edge at different frequencies and vibrating amplitudes. Therm Sci. https://doi.org/10.2298/tsci230715235c

Doinikov AA et al (2020a) Acoustic radiation forces produced by sharp-edge structures in microfluidic systems. Phys Rev Lett 124:154501–154501

Doinikov AA et al (2020b) Acoustic streaming produced by sharp-edge structures in microfluidic devices. Microfluid Nanofluid 24:1–13

Dong Z et al (2017) Mixing and residence time distribution in ultrasonic microreactors. AIChE J 63:1404–1418

Elvira KS, Solvas IXC, Wootton RCR, de Mello AJ (2013) The past, present and potential for microfluidic reactor technology in chemical synthesis. Nat Chem 5:905–915

Harley SW, Kolesnik K, Heath DE, Collins JD (2024) Enhanced acoustic streaming effects via sharp-edged 3D microstructures. Lab Chip 24:1626–1635

Holdich RG (2002) Fundamentals of particle technology. Midland Information Technology & Publishing, Shepshed

Huang P-H et al (2013) An acoustofluidic micromixer based on oscillating sidewall sharp-edges. Lab Chip 13:3847–3852

Huang P-H et al (2018) A sharp-edge-based acoustofluidic chemical signal generator. Lab Chip 18:1411–1421

Jalal J, Leong TSH (2018) Microstreaming and its role in applications: a mini-review. Fluids 3:93

Karlsen JT, Bruus H (2015) Forces acting on a small particle in an acoustical field in a thermoviscous fluid. Phys Rev E 92:043010

Kaynak M et al (2017) Acoustic actuation of bioinspired microswimmers. Lab Chip 17:395–400

Khasi S, Fayazi A, Kantzas A (2021) Effects of acoustic stimulation on fluid flow in porous media. Energy Fuels 35:17580–17601

Laurell T, Lenshof A (eds) (2014) Microscale acoustofluidics. Royal Society of Chemistry, Cambridge

Li W, Vigil RD, Beresnev IA, Iassonov P, Ewing R (2005) Vibration-induced mobilization of trapped oil ganglia in porous media: experimental validation of a capillary-physics mechanism. J Colloid Interface Sci 289:193–199

Lieu VH, House TA, Schwartz DT (2012) Hydrodynamic tweezers: impact of design geometry on flow and microparticle trapping. Anal Chem 84:1963–1968

Lighthill SJ (1978) Acoustic streaming. J Sound Vib 61:391–418

Ma Z et al (2020) Ultrasonic microstreaming for complex-trajectory transport and rotation of single particles and cells. Lab Chip 20:2947–2953

Miah MdAK, Zeller P, Olsen MG, Juárez JJ (2023) Acoustic driven circulation around cylindrical obstructions in microchannels. Phys Fluids 35:111701

Nama N, Huang P-H, Huang TJ, Costanzo F (2014) Investigation of acoustic streaming patterns around oscillating sharp edges. Lab Chip 14:2824–2836

Ng JW, Collins DJ, Devendran C, Ai Y, Neild A (2016) Flow-rate-insensitive deterministic particle sorting using a combination of travelling and standing surface acoustic waves. Microfluid Nanofluid 20:151

Olsen MG, Adrian RJ (2000) Out-of-focus effects on particle image visibility and correlation in microscopic particle image velocimetry. Exp Fluids 29:S166–S174

Otumudia E, Hamidi H, Jadhawar P, Wu K (2022) The utilization of ultrasound for improving oil recovery and formation damage remediation in petroleum reservoirs: review of most recent researches. Energies 15:4906

Ovchinnikov M, Zhou J, Yalamanchili S (2014) Acoustic streaming of a sharp edge. J Acoust Soc Am 136:22–29

Pavlic A, Roth L, Harshbarger CL, Dual J (2023) Efficient modeling of sharp-edge acoustofluidics. Front Phys. https://doi.org/10.3389/fphy.2023.1182532

Pothuri C, Azharudeen M, Subramani K (2019) Rapid mixing in microchannel using standing bulk acoustic waves. Phys Fluids 31:122001

Raffel M, Willert CE, Wereley ST, Kompenhans J (2007) Particle image velocimetry: a practical guide. Springer, Berlin, Heidelberg. https://doi.org/10.1007/978-3-540-72308-0

Thielicke W, Sonntag R (2021) Particle image velocimetry for MATLAB: accuracy and enhanced algorithms in PIVlab. J Open Res Softw 9:12

Thielicke W, Stamhuis EJ (2014) PIVlab—towards user-friendly, affordable and accurate digital particle image velocimetry in MATLAB. J Open Res Softw 2:30

Vainshtein P, Fichman M, Gutfinger C (1995) Acoustic enhancement of heat transfer between two parallel plates. Int J Heat Mass Transf 38:1893–1899

Wang Z et al (2019) Cell lysis via acoustically oscillating sharp edges. Lab Chip 19:4021–4032

Wei W, Wang Y, Wang Z, Duan X (2023) Microscale acoustic streaming for biomedical and bioanalytical applications. TrAC Trends Anal Chem 160:116958

Westerweel J (1997) Fundamentals of digital particle image velocimetry. Meas Sci Technol 8:1379

Yeh H-L, Juárez JJ (2019) Oil phase displacement by acoustic streaming in a reservoir-on-a-chip. Microfluid Nanofluid 23:113

Yeh H-L, Juárez JJ (2021) Ultrasound-enhanced diffusion and streaming of colloids in porous media. Exp Therm Fluid Sci 121:110282

Zhang C, Guo X, Brunet P, Costalonga M, Royon L (2019a) Acoustic streaming near a sharp structure and its mixing performance characterization. Microfluid Nanofluid 23:104

Zhang C et al (2019b) Acoustic streaming near a sharp structure and its mixing performance characterization. Microfluid Nanofluid 23:1–15

Zhang C et al (2020a) Acoustic streaming generated by sharp edges: the coupled influences of liquid viscosity and acoustic frequency. Micromachines 11:607

Zhang C, Guo X, Royon L, Brunet P (2020b) Unveiling of the mechanisms of acoustic streaming induced by sharp edges. Phys Rev E 102:043110

Zhang C et al (2020c) Mixing intensification using sound-driven micromixer with sharp edges. Chem Eng J 410:128252